Jet-like features near the nucleus of Chiron

J. L. Elliot*†‡, C. B. Olkin*‡, E. W. Dunham§, C. H. Ford‖, D. K. Gilmore¶, D. Kurtz#, D. Lazzaro, D. M. Rank¶, P. Temi¶, R. M. Bandyopadhyay*, J. Barroso**, A. Barucci††, A. S. Bosh‡, M. W. Bule‡, S. J. Bus*, C. C. Dahn‡‡, D. W. Foryta§§, W. B. Hubbard‖‖, D. F. Lopes**, R. L. Marcialis‖‖¶¶, S. W. McDonald*, R. L. Millis‡, H. Reitsema##, D. G. Schleicher‡, B. Sicardy†††***, R. P. S. Stone††† & L. H. Wasserman‡**

CONSIDERED as a comet, the object 2060 Chiron is unusual in two respects: it exhibits outbursts at very large distances from the Sun[1–3], and its nucleus is much larger than that of any other known comet[4,5]. It is, however, similar in size to the recently discovered Kuiper-belt objects[6]—a population of objects with orbits beyond Neptune, which are a possible source of short-period comets. This has led to the conjecture that Chiron is related to these objects, but its chaotic orbit has brought it much closer to the Sun[7]. Here we report observations of a recent stellar occultation by Chiron which permit the identification of several features associated with Chiron's coma. The observation of discrete, jet-like features provides evidence that the coma material originates from just a few, small active areas, rather than from uniform sublimation, and that the particles in at least one of these features have radii greater than 0.25 μm. The observations also suggest the presence of material in the plane of Chiron's orbit and are consistent with a gravitationally bound coma. Finally, the present data, and those from a previous occultation[8], constrain the radius of Chiron to lie between 83 and 156 km.

The 9 March 1994 occultation of Ch08 (GSC248 − 01674)[9] by Chiron was successfully observed with two telescopes: the 0.9-m telescope aboard NASA's Kuiper Airborne Observatory (KAO) flying near Recife, Brazil and the 0.5-m telescope at the South African Astronomical Observatory (SAAO) at Sutherland. We attempted observations with five other telescopes in Brazil. But their positions turned out to be far from the final predicted shadow path of Chiron, and all were clouded out. Instrumental parameters for the observations are specified in Table 1. Compared with its photometric history[2], Chiron was relatively faint at the time of our observations, with a standard magnitude[10] $H_V = 6.6 \pm 0.1$.

We generated a light curve from the KAO optical data using the technique of point-spread-function (PSF) model fitting. The infrared light curve was produced by doing aperture photometry with a synthetic aperture three pixels in radius (image radii ranged between 1.0 and 2.0 pixels). The SAAO light curve was obtained directly from the recorded photomultiplier-tube integrations. Sections of the light curves that bracket Chiron's closest approach to the star are shown in Fig. 1. A sharp drop and recovery occurs in all light curves, which we shall denote as feature 1 (F1). This appears similar to a feature in the Palomar light curve for the earlier Chiron occultation—one interpretation of which is a dust jet[8]. In addition, broader and shallower occultation features are particularly evident in the KAO optical light curve. To show the occultation features more clearly, shorter sections of the light curves are shown in Fig. 1, right panel.

In addition to F1 in the KAO optical light curve, we also see a broader feature (F2), that has a full-width at half-maximum (FWHM) of ~74 km, but less optical depth. Due to lower signal-to-noise ratio, F2 is not detectable in the infrared or SAAO light curves (although there is a hint of it in the former). Also, we note in the KAO optical light curve a low-level attenuation of the stellar signal that begins at ~517 s after the reference time and a similar attenuation between F1 and F2. Noting that F2 has a steeper slope on its leading edge than its trailing edge, one could interpret F2 as a symmetrical feature embedded in a low-level attenuation that ends at the trailing edge of F2. Without knowing how to apportion the optical depth into real, physical features, we have taken the liberty of labelling F3 as a feature that begins with the first low-level attenuation and ends at the trailing edge of F2. Finally, a feature labelled F4 is present in the KAO optical light curve. Its significance is 3σ (well below the detection limits of Earth-based imaging), and it occurs when the star aligns with Chiron's orbit plane, where material may be expected. Table 2 gives information about the optical depths and widths of the features.

To establish the geometrical relationship of these features in the light curves to the nucleus of Chiron, in Fig. 2 we have plotted a Chiron-centred sky frame[11] that shows the orbit plane, the track of the star from both stations, and the direction to the Sun. Because Chiron was only 15° from opposition, the largest component of the vector to the Sun is actually perpendicular to the plane of Fig. 2. The relative position of the star and Chiron's centre of light (assumed to be the centre of the nucleus) was determined from 40 astrometric frames taken with the 61-inch astrometric reflector at the US Naval Observatory, which yielded formal errors (1σ) of ±16 km in right ascension and declination (the f, g coordinate systems in Fig. 2). The broad, low-optical-depth feature (F3) is nearly symmetrical around the closest approach time of the event, and F4 occurs near the orbit-plane crossing for the KAO (at 575 ± 5 s after 23:20:01 UT—the uncertainty is larger than the uncertainty in the closest approach owing to the oblique intersection of the apparent star path with the orbit plane).

We can argue against the possibility that F1 is the signature of a small, sharp-edged body or that of a grazing occultation by the nucleus. Although a small body (or the nucleus) could produce a partial occultation, its characteristic dimensions would be of the order of the Fresnel diffraction scale $\sqrt{\lambda D}$, where λ is the wavelength of observation and D is the body–observer distance. These values are 0.9 and 1.6 km for the optical and infrared data respectively (the projected angular diameter of the star at Chiron's distance would be even less, only 0.1 km). The wings of F1 in the KAO optical light curve are much broader than this, ruling out a solid body or nuclear occultation (unless either of these were surrounded by a dust cloud that produced the wings).

Accepting that F1 is not a partial nuclear occultation, we can place a 3σ upper limit on Chiron's radius of 156 km from our closest approach distance of 108 ± 16 km. Compare this with the 83 km lower limit on Chiron's radius derived from the previous stellar occultation[8] and radii ranging between 74 ± 11 km and 104 ± 10 km from thermal infrared observations[5].

Other possibilities for F1 would be a suborbital arch, dust jet, or shell—the last two of which are seen in the comae of comets[12] and emanating from the nucleus of comet Halley[13,14]. This interpretation would be consistent with the smooth appearance of the coma from ground-based imaging[15–17], as all features we see would not be resolved in those data. The interpretation of F1 as caused by the outflow from a conical jet requires a spreading angle of ~12° for our nominal geometrical solution and a nuclear

* Department of Earth, Atmospheric and Planetary Sciences, Massachusetts Institute of Technology, Cambridge, Massachusetts 02139-4307, USA. † Department of Physics, Massachusetts Institute of Technology, Cambridge, Massachusetts 02139-4307, USA. ‡ Lowell Observatory, Flagstaff, Arizona 86001, USA. § NASA Ames Research Center, Space Science, MS 245-6, Moffett Field, California 94035-1000, USA. ‖ SETI Institute, 2035 Landings Drive, Mountain View, California 94043, USA. ¶ University of California, Lick Observatory, Santa Cruz, California 95064, USA. # University of Cape Town, Private Bag, Rondebosch 7700, Cape Town, South Africa. ** CNPq/Observatório Nacional, DAF, 20921 Rio de Janeiro, Brazil. †† Observatoire de Paris, 92195 Meudon Cédex Principal, France. ‡‡ US Naval Observatory, PO Box 1149, Flagstaff, Arizona 86002-1149, USA. §§ UFPR/Dep. Fisica, Centro Politecnico, 80000 Curitiba, Brazil. ‖‖ Lunar and Planetary Laboratory, University of Arizona, Tucson, Arizona 85721, USA. ¶¶ Pima Community College, 2202 West Anklam Road, Tucson, Arizona 85709, USA. ## Ball Aerospace, PO Box 1062, Boulder, Colorado 80306-1062, USA. *** Université Paris 6, UFR physique 924, 75252 Paris Cedex 05, France. ††† Lick Observatory, Mount Hamilton, California 95140, USA.

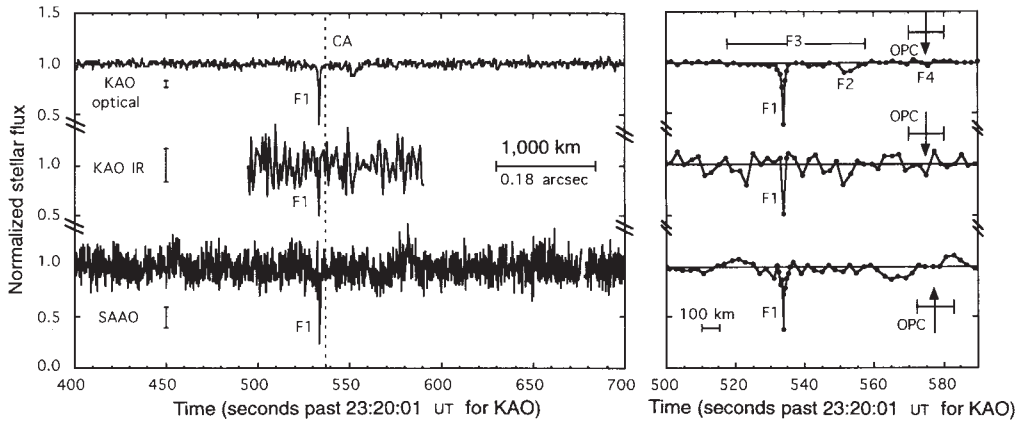

FIG. 1 Chiron occultation light curves. Portions of the stellar flux (normalized to 1.0 for the unocculted star) from Ch08 have been plotted versus UT for an interval that includes Chiron's closest approach to Ch08 (shown by the dotted line labelled "CA"). The left-hand panel is at full resolution. The right-hand panel includes only data near closest approach; to enhance the signal-to-noise ratio, data outside the sharp drop (feature 1, F1) have been averaged to 2.0 s. The segment of the light curves comprising F1 have been left at full resolution for the KAO data, whereas the SAAO data have been averaged to 0.4 s (two integration times and two deadtimes). In the left-hand panel the error bars are $\pm 1\sigma$, and the 1,000-km spatial scale at Chiron (for the KAO shadow velocity of 18.32 km s^{-1}) is approximately the resolution of the Hubble Space Telescope. The orbit-plane crossing (OPC) time is indicated in the right-hand panel. A sharp drop and recovery (F1) is evident in all three light curves. As the paths of the KAO and SAAO were separated in Chiron's shadow plane by only 1.4 km at closest approach (107.8 km for the KAO and 106.4 km for SAAO), we have assumed that F1 was caused by the same material for both stations. We therefore corrected for the unknown timing offset in the SAAO data by retarding the time axis of the light curve by 309.9 s to align the sharp feature with that of the KAO. Near 680 s, there is a gap in the SAAO light curve, where a noise spike was removed. These spikes reached a flux level 100% above the Ch08 level and were removed before calculating the unocculted level for Ch08. See text for description of the features.

radius of 83 km (ref. 8), if we assume that the jet originates on the limb in the sky plane and from a small active area on the surface—consistent with the 1–2 km radii for active areas that would have been required to produce the visible coma at earlier times[3,16–18]. Larger and smaller spreading angles are possible for other assumptions.

The ratio of extinction at infrared to that at optical wavelengths for F1 is formally 1.31 ± 0.65 (over equal integration intervals of 1.0 s). For the particle-size distributions found for comet Halley ($n^{\alpha}dn$, with α between -4 for particles with radii of $\sim$100 μm and -1.54 for those with radii $\sim$0.1 μm)[19], this ratio would be much less than one. Hence the extinction in F1 can not be caused by this type of particle-size distribution, but must be dominated by large particles. To obtain some quantitative estimate of the lower limit on the particle size, we use Mie theory for spherical particles[20], and find that for various compositions from silicate to tholin to graphite these data are consistent with a lower limit of 0.25 μm (ref. 21) on the radius of particles. So most of the extinction we measure must be contributed by particles larger than this, but somewhat different limits would apply for non-spherical particles, with indices of refraction different from our assumption[20]. This conclusion for F1 shows a particle population differing from that measured[22] by the particle detectors on the Halley spacecraft, which found a significant population of particles with radii smaller than 0.25 μm. The material probed here, however, is from a different object, much further from the Sun, and sampled much closer to the nucleus. An upper limit to the radii of particles that can be lifted from the nucleus by escaping gas has been estimated[17] at 100 μm for CO and 10 μm for CO_2.

TABLE 1 Observations of the Ch08 occultation by Chiron

Telescope (diameter)	Detector	Filter	Recording interval (UT)	Number of integrations	Integration time (s)	S/N (for 1 s)	S/N (for 10 km)
KAO (0.9 m)	CCD	None*	23:20:01–23:36:40.5	2,000	0.5	52	38
KAO (0.9 m)	HgCdTe array	K	23:20:01–23:36:40.5	1,000	1.0	5.8	4.3
SAAO (0.5 m)	PMT	V	22:58:53–23:42:40†	13,266	0.1†	20	15

The occulted star is the brighter of two stars that have the combined photometric measurements: $V = 11.95$ mag, $(B-V) = 0.92$, $(V-R) = 0.42$, $(V-I) = 0.86$, $(V-K) = 1.9$. The fainter companion star lies at a distance of 3.27 arcsec from the brighter one, at a position angle of 19.6°, and it has magnitude differences with Ch08 of 2.15 in the K band and 3.83 in a broadband red filter (6,600–8,300 Å), used by the US Naval Observatory. The KAO optical data were recorded with a high-speed CCD (charge-coupled device) photometer[24], using two 60 × 60 pixel subframes (0.98 arcsec per pixel): one subframe contained the merged images of Chiron, Ch08 and the faint companion star; the other contained a field star of brightness comparable to Ch08 and 4.38 arcmin away. A continuous series of 2,000 subframe pairs were recorded, and the timing of the series was related to UT with a GPS clock. A beamsplitter enabled simultaneous infrared observations to be carried out with a NICMOS HgCdTe array (128 × 128 pixels, ~1.4 arcsec per pixel) that was read out once per second, synchronously with the optical data recording. The SAAO data were recorded with a photomultiplier tube (PMT) at an integration time of 0.1 s, through an aperture 30 arcsec in diameter. Reference to the standard star HR4064 showed that the night was photometric at SAAO. The deadtime between integrations was usually 0.1 s, but, sometimes it was 0.0 s, which made it impossible to accurately relate the recording times of these data to UT. The signal-to-noise ratio S/N in the next to last column is defined as the ratio of the unocculted flux of the star to the r.m.s. noise, each integrated for one second. The last column contains the analogous ratio for a 10 km interval in the sky-plane.

* The unfiltered CCD response and stellar spectrum combine for a mean wavelength of ~0.68 μm.

† The end time of the SAAO data is not precisely known. The value here was calculated for a deadtime of 0.1 s between integrations for 98% of the data, and no deadtime between the remaining 2% of the integrations (as the deadtime between successive integrations was 0.1 s about 98% of the time and 0.0 s for the remaining 2%).

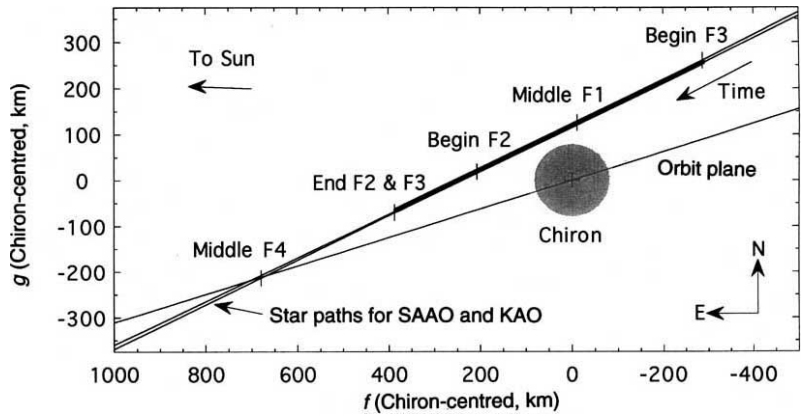

FIG. 2 The Chiron-centred sky-plane. Chiron's shadow at Earth is indicated in the (f, g) coordinate system[11], in which f is parallel to right ascension and g is parallel to declination. The orbit plane of Chiron has been plotted for reference. Along the paths probed by Ch08 as seen from the KAO and SAAO, relevant times for light-curve features are indicated, and time increases to the south-east. Note that the occultation probed the orbit plane ahead of Chiron. Along the apparent path of the star, we have indicated the positions of the features derived from the KAO optical light curve. Coincidentally both stations probed nearly the same region near Chiron. The uncertainty in the closest approach time is the geometrical error divided by the shadow velocity (~0.9 s). Chiron was 15° from opposition at the occultation time, so the vector to the Sun is mostly out of the plane of the figure. A Chiron radius of 83 km has been assumed[8] (indicated by the shaded circle). For the KAO, the occultation shadow probes the orbit plane at 575 s after 23:20:01 UT, and there is a 3σ occultation feature evident in the light curve at this time (F4). If F1 and F2 are caused by jets originating from the limb of the nucleus nearest to where these features were detected, then extending lines from F1 and F2 to Chiron's centre, we see that F2 would be on the side of the nucleus facing the Sun (consistent with the jet hypothesis) and F1 would be on the sunrise or sunset limb (marginally consistent with the jet hypothesis). Owing to projection effects, however, either feature could be connected to a sunlit or dark portion of the nucleus. Note that F3 is nearly symmetrical with respect to Chiron, as would be expected for a bound coma. At closest approach, Chiron was 8.83 AU from the Sun and 7.87 AU from the Earth.

If one interprets F1 as a jet, it is natural to interpret F2 as a jet also. Being probed further from the nucleus than F1, it has spread into a broader morphology. In fact, it is possible that F1 and F2 are caused by a single structure—shaped as a spiral or suborbital arch—that has been probed twice. In order to test this hypothesis, one would need to know the rotation of the nucleus. Although the period has been measured quite accurately[2,3,17], the direction of the rotation pole[23], estimated from the imaged coma morphology, disagrees somewhat with constraints from photometry[2]. Because we are seeing these features projected onto a plane, however, their distances from the nucleus in this plane are only lower limits on their true distances. Furthermore, the vector to the Sun points mostly out of the sky plane, so that either F1 or F2 could be emanating from a sunlit or dark side of the nucleus. Despite these uncertainties, we presently feel that F1 and F2 are probably caused by two distinct dust jets from the nucleus.

Although F3 is much broader, it could possibly be a jet, shell, or other shape[12]—seen much further from the nucleus than F1 or F2, but appearing nearly symmetrical with respect to the nucleus owing to projection effects. Another, and perhaps more plausible, explanation for F3 is that it is a symmetrical cloud of dust around the nucleus. If this material is flowing out uniformly at the speed of sound for CO (160 m s^{-1})[17], then the material rate of loss (for particles 10 μm in radius and density 1 g cm^{-3}) would be several orders of magnitude larger than that needed to account for the extended coma (in 1990, when Chiron was at least 0.5 mag brighter in H_V)[16,17,23]. Therefore we believe that the material causing F3 is not flowing outwards from the nucleus at the speed of sound, but is possibly gravitationally bound to the nucleus—a bound coma[16,17]. Such a feature would be unique to Chiron because it is the only known comet large enough for gravity to hold dust in bound orbits for periods ranging from tens of days[18] to a year[16]. If F3 is a manifestation of a bound

TABLE 2 Material detected near Chiron

Feature	Light curve	Midtime (s after 23:20:01 UT)	Distance from Chiron's centre (km)*	Averaging interval (km)	Maximum optical depth measured	FWHM (km)	Integrated optical depth (km)†	Morphology
1	KAO, optical	533.7	126±16	9.2	0.92±0.07‡	5.5–9.2	13.2±1.3	Narrow, deep, symmetrical
	KAO, infrared			18.3	0.68±0.34	9.0–18.3	12.4±6.2	
	SAAO			7.3	0.98±0.46	4.5–7.3	7.2±3.4	
2	KAO, optical	552.4	295±16	Model fit	0.11±0.02	74±15	4.1±1.3	Asymmetric?
3	KAO, optical	537.4	108±16	Model fit	0.027±0.006	513±169	21.6±5.0	Broad, flat
4	KAO, optical	575.7	712±16	Model fit	0.07±0.04	12±10	1.6±0.5	3σ

The averaging interval is equal to the product of the apparent shadow velocity from the site and the integration interval for the data, and the maximum measured optical depth is derived from the integration having the lowest signal level. The differences between the integrated optical depth in the SAAO and KAO optical light curves can be attributed to one or more of the following: (1) the core of feature (F1) is not resolved in the KAO optical light curve, because the integration time is longer than for SAAO, (2) the duty cycle of the SAAO data recording is 50%, whereas that for the KAO data is 100%, or (3) F1 changed during the 310 s that elapsed between the recording of F1 at the two stations. The maximum optical depths and widths of F2, F3 and F4 were determined from fitting a lorentzian model.

* Distance of feature from Chiron's centre probed at midtime (column 3).

† The integrated optical depths depend on how one chooses to separate the features. For features 1 and 2 (F1 and F2) of the KAO optical light curve, the integrated optical depth was determined by taking the logarithm of the summed normalized stellar flux for all points in the feature (after correcting for the optical depth per point from F3 of 0.027). This optical depth was then converted to kilometres by multiplying by the velocity and integration time. For F3 the integrated optical depth was determined by model fitting (to include the optical depth contribution when this feature is embedded in the other features). The integrated optical depth for F4 was also determined by model fitting. Finally, the integrated optical depths for the KAO infrared and the SAAO data were calculated by multiplying the maximum optical depth by the averaging interval, with the SAAO data averaged over two points (for a time interval of 0.4 s, including the deadtime).

‡ Optical depth averaged over 18.3 km of projected width for feature 1 is 0.52±0.03. This average should be used when comparing with the average optical depth in the infrared. The extinction ratio (infrared to optical) is 1.31±0.65.

coma, it may be only a small part, with the remainder having too low an optical depth to be detectable in these data. □

Received 15 August; accepted 24 November 1994.

1. Tholen, D. J., Hartmann, W. K. & Cruikshank, D. P. *IAU Circ. No.* 4554 (1988).
2. Marcialis, R. L. & Buratti, B. J. *Icarus* **104,** 234–243 (1993).
3. Bus, S. J., Bowell, E., Harris, A. W. & Hewitt, A. V. *Icarus* **77,** 223–238 (1989).
4. Sykes, M. V. & Walker, R. G. *Science* **251,** 777–780 (1991).
5. Campins, H. *et al. Astr. J.* **108,** 2318–2322 (1994).
6. Jewitt, D. & Luu, J. *Nature* **362,** 730–732 (1993).
7. Scholl, H. *Icarus* **40,** 345–349 (1979).
8. Buie, M. W. *IAU Circ. No.* 5898 (1993).
9. Bus, S. J., Wasserman, L. H. & Elliot, J. L. *Astr. J.* **107,** 1814–1824 (1994).
10. Bowell, E. *et al.* in *Asteroids II* (eds Binzel, R. P., Gehrels, T. & Matthews, M. S.) (Univ. Arizona Press, Tucson, 1989).
11. Elliot, J. L. *et al. Astr. J.* **106,** 2544–2572 (1993).
12. Sekanina, Z. in *Comets in the Post-Halley Era* (eds Newburn, R. L., Neugebauer, M. & Rahe, J.) 769–823 (Kluwer, Dordrecht, 1991).
13. Sagdeev, R. Z. *et al. Nature* **321,** 262–266 (1986).
14. Sekanina, Z. & Larson, S. M. *Nature* **321,** 357–361 (1986).
15. West, R. M. *Astr. Astrophys.* **241,** 635–645 (1991).
16. Meech, K. J. & Belton, M. J. S. *Astr. J.* **100,** 1323–1338 (1990).
17. Luu, J. X. & Jewitt, D. C. *Astr. J.* **100,** 913–932 (1990).
18. Stern, S. A., Jackson, A. A. & Boice, D. C. *Astr. J.* **107,** 765–771 (1994).
19. Lamy, P. L., Grün, E. & Perrin, J. M. *Astr. Astrophys.* **187,** 767–773 (1987).
20. van de Hulst, H. C. *Light Scattering by Small Particles* (Dover, New York, 1981).
21. Olkin, C. B. *et al.* in *Proc. Airborne Astronomy Symp. on the Galactic Ecosystem: From Gas to Stars to Dust* (eds Haas, M. R., Davidson, J. A. & Erickson, E. F.) (Astr. Soc. Pacif., San Francisco, 1994).
22. McDonnell, J. A. M., Lamy, P. L. & Pankiewicz, G. S. in *Comets in the Post-Halley Era* (eds Newburn, R. L., Neugebauer, M. & Rahe, J.) 1043–1073 (Kluwer, Dordrecht, 1991).
23. Fulle, M. *Astr. Astrophys.* **282,** 980–988 (1994).
24. Buie, M. W. *et al. Bull. Am. Astro. Soc.* **25,** 1115 (1993).

ACKNOWLEDGEMENTS. We thank the entire KAO crew for their outstanding work, especially mission director J. McClenahan and navigator R. Morrison; we also thank the members of the Brazilian and US governments who worked out agreements that allowed KAO to use Brazilian air space and airport accommodation on short notice. The NICMOSII FPA used in these observations was donated by Rockwell International Science Centre. This work was supported in part by NASA.

Graft copolymers that exhibit temperature-induced phase transitions over a wide range of pH

Guohua Chen & Allan S. Hoffman*

Center for Bioengineering, FL-20, University of Washington, Seattle, Washington 98195, USA

THERE are many potential applications of 'intelligent' aqueous polymer systems[1–8] in medicine, biotechnology, industry and in environmental problems[9–13]. Many of these polymer systems undergo reversible phase transitions—for example, abrupt changes in volume—in response to external stimuli such as temperature, pH or the nature of the solvent. Most of the polymers studied previously are responsive to only one kind of stimulus. But for some applications, independent responsiveness to several factors, such as temperature and pH, may be required. Here we describe a polymer that undergoes marked solubility changes in water in response to temperature and/or pH changes. The polymer is prepared by grafting temperature-sensitive side chains onto a pH-sensitive backbone. We also find that block copolymers, in which the temperature- and pH-sensitive units alternate along the chain, show similar behaviour.

When the temperature of a polymer solution is raised above the lower critical solution temperature (LCST) or cloud point (CP), the polymer will phase-separate[14]: hydrophobic groups in the polymer form insoluble aggregates, turning the solution cloudy. We have used this principle previously[15] to prepare a copolymer hydrogel which exhibits temperature-sensitive swelling–deswelling changes over a limited pH range. This gel is composed of a random copolymer of monomers that are pH-sensitive (acrylic acid, AAc) and temperature-sensitive (*N*-isopropyl acrylamide, NIPAAm). For a composition of less than 10 mol% AAc, the gel exhibits a CP at pH 7.4. For higher AAc content the CP disappears, because then the AAc components (which are ionized at pH 7.4) convey sufficient solubility to offset the aggregation of the hydrophobic temperature-sensitive components. High molecular weight PAAc is a well-known bioadhesive polymer, which 'sticks' to the hydrated mucosal cells coating the eye, nose, mouth, lungs, gastrointestinal tract, vagina and anus. In order to prolong the residence time of a drug delivery vehicle in contact with such mucosal surfaces, PAAc is often incorporated into a delivery formulation. Further, if it is also desirable to slow the rate of drug release from the bioadhesive formulation, a more hydrophobic component, such as the temperature-sensitive polymer, may be added. Random copolymers of AAc and NIPAAm will not work, because of the loss of the temperature sensitivity when the content (that is, molecular weight) of the AAc component is increased to the point where bioadhesive properties are obtained. Physical mixtures of these two types of polymers are also possible, but they tend to separate physically and release drug too rapidly. Thus, the graft copolymer structure, which combines both behaviours in a single molecule and does not permit physical separation, is most effective. This is the rationale for the work described here.

Copolymers[16] and interpenetrating networks[17] of two polymers that form hydrogen-bonded complexes involving carboxylic acid groups may also exhibit temperature sensitivity, but this usually disappears when the pH is raised above the pK of the acid groups, ionizing them to carboxylate. For example, Klier *et al.*[16] prepared hydrogels of graft copolymers of polyethyleneglycol (PEG) on a poly(methacrylic acid) (PMAAc) backbone, which form hydrogen-bonded complexes between –O– and –COOH groups at low pH. Although these gels gradually shrank as temperature was raised at pH 4, this temperature-sensitivity would not occur at pH 7.4 where the gels were highly swollen owing to ionization of the carboxyl groups and the consequent disruption of the complex[16].

To obtain polymers that retain their temperature-induced transition over broad and useful compositional and pH ranges, especially at physiological conditions of pH 7.4 in a saline solution, we have synthesized graft copolymers composed of side-chains of a temperature-sensitive polymer (PNIPAAm) grafted onto a pH-sensitive backbone polymer (PAAc). We have used two methods for synthesizing the NIPAAm-g-AAc graft copolymers (Fig. 1*a–d*). In Fig. 1*e* we illustrate possible hydrogen-bonding interactions between the grafted NIPAAm and backbone AAc groups; these hydrogen-bonded structures are similar to those proposed to exist between carboxyl and amide groups in interpenetrating networks of PAAc and an acrylamide copolymer[17].

In Fig. 2 we plot the effect of AAc content on CP for random and graft copolymers of NIPAAm and AAc at pH 7.4 and 4.0; that is, above and below the pK of AAc, respectively. It can be seen that the CP of the random copolymer is always higher than that of the PNIPAAm homopolymer and rapidly rises as the AAc content increases, especially at pH 7.4. In contrast, the graft copolymers show a constant CP at either pH, independent of AAc content over a wide range of compositions. Their LCST may rise only when the composition of the graft approaches 100% AAc (assuming that the few PNIPAAm graft chains present will still phase-separate individually, but without any visible evidence of turbidity in the solution). This constancy of CP over a broad composition range (especially at pH 7.4) is a clear demonstration of the significant differences in behaviour between the random and graft copolymers studied here, as well as between our graft copolymers and those of Klier *et al.*[16] or the interpenetrating networks of Katono *et al.*[17].

* To whom correspondence should be addressed.